Arabian Journal of Chemistry (2020) 13, 1429–1439

King Saud University

Arabian Journal of Chemistry

www.ksu.edu.sa
www.sciencedirect.com

ORIGINAL ARTICLE

Design and development a novel uranyl sensor based on FePt/$ZnIn_2S_4$ core-shell semiconductor nanostructures

Hossein Zeynali [a,*], Mohammadhassan Motaghedifard [b,*], B.F.O. Costa [c], Hossein Akbari [d], Zohreh Moghadam [e], Morteza Babaeianfar [a], Mohammad Javad Rashidi [a]

[a] *Department of Physics, Kashan Branch, Islamic Azad University, Kashan, Iran*
[b] *Young Researchers and Elites Club, Qom Branch, Islamic Azad University, Qom, Iran*
[c] *CFisUC, Physics Department, University of Coimbra, P-3004-516 Coimbra, Portugal*
[d] *Department of Physics, Ardabil Branch, Islamic Azad University, Ardabil, Iran*
[e] *Department of Analytical Chemistry, Faculty of Chemistry, University of Kashan, Kashan 87317-51167, Iran*

Received 25 September 2017; accepted 17 November 2017
Available online 2 December 2017

KEYWORDS

Core-shell nanostructures;
Solvothermal process;
Magnetization behavior;
Uranyl glue;
Electrochemical study

Abstract In this study, the FePt core, $ZnIn_2S_4$ shell and FePt-$ZnIn_2S_4$ core-shell nanostructures were successfully synthesized using solvothermal process. Temperature dependent hysteresis behavior of as-synthesized nanoparticles (NPs) FePt and FePt/$ZnIn_2S_4$ showed super paramagnetic response at 300 K and ferromagnetic properties with a coercive field (H_c) of 2830 Oe and 970 Oe at 2 K, respectively. Also, the blocking temperature (T_B) estimating by the peak in ZFC curves was about 26 K for FePt and about 46 K for FePt/$ZnIn_2S_4$ NPs. After the identification process of nanostructure, using electrochemical methods, the behavior of FePt-$ZnIn_2S_4$ core-shell@PGE was studied in 0.1 M phosphate buffer solution (PBS) containing 5.0 mM $[Fe(CN)_6]^{3-/4-}$. The EIS complex plane plots showed a drastic change in the charge transfer resistance of the probe redox reaction as a function of UO_2^{2+} concentration. This behavior was used for construction of the calibration curve, and a linear range from 0.5 to 10.0 μM UO_2^{2+} with a detection limit of 71.7 nM.

* Corresponding authors.
E-mail addresses: zeynali.ph@gmail.com (H. Zeynali), mhmf1359@yahoo.com (M. Motaghedifard).

Peer review under responsibility of King Saud University.

Production and hosting by Elsevier

1. Introduction

In the last decade, there has been a growing high interest in one-dimensional nanostructures such as nanofibers, (Cheng et al., 2014), nanobelts (Xing et al., 2011), nanotubes (Chi et al., 2014), and nanorods (Carvajal et al., 2014; Khayatian et al., 2014), because of their unique properties and potential

https://doi.org/10.1016/j.arabjc.2017.11.014
1878-5352

applications in many fields (Cheng et al., 2014; Xing et al., 2011; Chi et al., 2014; Carvajal et al., 2014; Khayatian et al., 2014; Wang et al., 2013; Hieu et al., 2014). Metal nanomaterials exhibit many unique electronic, optical, catalytic properties that are different from those of the corresponding bulk metal materials (Dotzauer et al., 2006). Because of advantages such as high catalytic activities, efficient electron transfer rate, large specific surface area and good chemical stability of the metal nano- materials (Yan et al., 2001; Balamurugan et al., 2011), in recent years, many researchers have developed electrochemical sensors based on nanoparticles. Recently, hybrid nanomaterials having core-shell structures based on shells such as $ZnIn_2S_4$ have started gaining attention of researchers in sensor technologies (Shim et al., 2013).

The only member of the AB_2X_4 family of semiconductors with a layered structure, $ZnIn_2S_4$ has been extensively studied because of its important potential uses in charge storage, electrochemical recording, thermoelectricity, and photocatalysis especially (Lei et al., 2003; Romeo et al., 1973; Seo et al., 1999). Various physical and chemical methods have been developed to prepare hybrid metal based nanoparticles of $ZnIn_2S_4$ such as nanosheet, nanotubes, nanoribbons, nanowires, and flower-like microspheres for solar water splitting (Peng et al., 2011; Chen et al., 2015; Zhou et al., 2013). On the other hand, many structures of $ZnIn_2S_4$ such as Cu, Co metal-doped $ZnIn_2S_4$ photocatalysts (Shen et al., 2008; Yuan et al., 2013), Multi-Walled Carbon Nanotubes/$ZnIn_2S_4$ (Chai et al., 2012), CdS/$ZnIn_2S_4$ (Yu et al., 2012), $CuInS_2$/$ZnIn_2S_4$ (Bozhko et al., 2013), In_2S_3/$ZnIn_2S_4$ (Mei et al., 2013), and Reduce Graphene Oxide/$ZnIn_2S_4$ (Zhou et al., 2013) have been synthesized which were been improved the photo catalytic activity of them in compare to $ZnIn_2S_4$.

In other side, the attachment of nanostructured $ZnIn_2S_4$ material with structurally well-defined morphology onto a conductive substrate has been difficult to achieve and remains as a challenge. This disadvantage imposes barriers in the construction of device because stronger binding of electrode films onto conductive substrate is a necessary prerequisite for the fabrication of devices, especially for solar cells. Therefore, in present work, in order to improve the catalytic activity and well-defined distribution of $ZnIn_2S_4$ nanoparticles on the surface of electrode, we report the synthesis of core-shell FePt-$ZnIn_2S_4$ composite by a novel solvothermal method. This preparation method can effectively make $ZnIn_2S_4$ nanoparticles distribute on the surface of FePt super paramagnetic/conductive nanostructures.

Uranium is a ubiquitous metal of special concern because of its high toxicity and radioactivity (Li and Zhang, 2012; Li et al., 2009). In the past half-century, uranium has been widely used in many fields such as nuclear power station, nuclear weapons, industrial and medical fields. Recently, its usage is increasing with the development of nuclear energy. Therefore, human beings have a high chance of being exposed to uranium, which can cause serious harms to human health (Fang et al., 2010). Therefore, the study of uranium has already become a hot research topic in many fields such as environmental science, biological science, medical science and toxicology.

The methods including inductively coupled plasma atomic emission spectrometry (ICPAES) (Fujino et al., 2000), inductively coupled plasma-mass spectrometry (ICP-MS) (Ejnik et al., 2000), ion chromatography (IC) (Grudpan et al., 1995) and capillary zone electrophoresis (CZE) (Lu et al., 1998), graphite furnace atomic absorption spectrometry (GFAAS) (Khan and Yasmin, 2003), fluorimetry (Hong et al., 1989), spectrophotometry (Khan et al., 2001), neutron activation analysis (Byrne and Benedik, 1988) and voltammetry (Davis and Gray, 1964) have been used for determination of uranium concentrations. However, these methods require expensive equipments and higher running cost and their availability is limited.

Among different strategies explored to reach this goal, electro analytical methods are simpler in means of equipment and expenditure and yet are potent tools for analysis of uranium in watery environments. Electro analysis has a major advantage over the aforementioned techniques, as it allows speciation of uranium in solution by direct measurement, and as such may generally be regarded as a nondestructive detection method.

According to our knowledge, no report has been published on determination of UO_2^{2+} using core-shell nanostructures based on electrochemical sensors. So, the purpose of this study was; (i) firstly, solvothermal synthesis of FePt-$ZnIn_2S_4$ core-shell nanostructures and its characterization; and in continuation, (ii) application of FePt-$ZnIn_2S_4$ core-shell@PGE as a new electrode for UO_2^{2+} monitoring in phosphate buffer solution.

2. Experimental

2.1. Materials and physical measurements

Platinum (II) acetyl acetonate (97%), tris (acetyl acetonato) iron (III) (99.9%), Indium(III) Nitrate Pentahydrate, In $(NO_3)_3{\cdot}5H_2O$ (99.9%), anhydrous ethyl alcohol and hexane were purchased from Merck and 1,2-hexadecanediol (90%), oleic acid (99%) and oleyl amine (70%), Thioacetamide (TAA, >99%) and Zinc acetyl acetonate hydrate powder, $Zn(acac)_2$ (99.9%), from Sigma-Aldrich. All the chemicals were used without further purification. X-ray diffraction (XRD) patterns were recorded by a Philips-X'PertPro, X-ray diffractometer using Ni-filtered Cu K_α radiation at scan range of $10 < 2\theta < 80$. The energy dispersive X-ray spectroscopy (EDXS) analysis was obtained on a Philips EM208 microscope. Transmission electron microscope (TEM) images were obtained on a Philips EM208S transmission electron microscope with an accelerating voltage of 100 kV.

The electrochemical studies were carried out using an Autolab potentiostat-galvanostat PGSTAT 35 (Ecochemie Utrecht, Netherlands), equipped with the GPES 4.9,006 software and FRA 4.9 software. The experiments were carried out in a three-electrode glass cell with Ag/AgCl (3.0 M KCl) as a reference electrode, a platinum wire as counter electrode and a pencil graphite electrode (PGE) as working electrode. The EIS measurements were done in a 5.0 mV ac amplitude potential superimposed on the formal potential of the redox probe ($E^{o\prime} = +0.250$ V) in a wide frequency range from 10 kHz to 100 mHz. All experiments were carried out at an ambient temperature of 25 ± 0.1 °C.

Magnetic measurements were done in a cryogenic free vibrating sample magnetometer operating using a closed-cycle *He* cryostat. The PPMS DynaCool (Quantum Design) in VSM option were used with a sensitivity of 0.016 mT,

operating magnetic field up to 9 T and temperature range of 1.8–300 K. Sample holders were cylindrical rods made of polypropylene with a diameter of about 3 mm. The sample occupies a height of about 2 mm inside the rod.

2.2. Synthesis of FePt core nanoparticle

Nuclear magnetic FePt nanoparticles as a core were synthesized using solvothermal method under standard airless process in accordance with the following command: initial precursors containing iron (III) acetylacetonate (0.50 mmol), platinum (II) acetylacetonate (0.25 mmol), 1,2-hexadecanediol (2.5 mmol), oleic acid (5.0 mmol), oleyl amine (5.0 mmol) were mixed in 10 mL benzyl ether and magnetically stirred for 20 min under a flow of N_2 atmosphere. Then the mixture was heated to boiling benzyl ether at a rate of approximately 5 °C/min and kept at this temperature for 15 min. After completion of the growth of nanoparticles, the heat source was separated from the reaction vessel allowing the mixture to cool at room temperature. The resulting black nanoparticles were isolated by adding 40 mL of ethanol and centrifugation. Then, the ethanol impurities were separated and black precipitation was dispersed in hexane in the presence of oleic acid and oleyl amine. In order to completely remove the extra impurities, the centrifugation was repeated twice. Finally, the FePt core nanoparticles were dispersed with the stabilizer in hexane.

2.3. Synthesis of $ZnIn_2S_4$ shell nanostructures

For synthesis of $ZnIn_2S_4$ nanostructures as a shell, stoichiometric quantities of thioacetic acid (TAA) (150 mg), In $(NO_3)_3{\cdot}5H_2O$ (300 mg), Zn $(acac)_2$ (130 mg), 1, 2 hexadecane diol (365 mg), oleic acid (1200 μL), oleyl amine (1225 μL) were mixed in 10 mL benzyl ether and magnetically stirred under a flow of N_2 atmosphere for 20 min at room temperature. Then, the resulting mixing was heated from 100 °C to boiling point of benzyl ether (300 °C) at a rate of approximately 5 °C/min. After the reaction, the heat source was removed from the reaction vessel allowing the mixture to cool at room temperature. Then, the resulting nanostructures were filtrated and separated by adding 40 ml of ethanol and centrifugation in 8000 rpm for 10 min. Finally, the nanostructures were dried in a vacuum oven at a temperature of 70 °C for two hours.

2.4. Synthesis of FePt-$ZnIn_2S_4$ core-shell nanostructures

The process for the synthesis of FePt-$ZnIn_2S_4$ core-shell nanostructures was done as following: based on stoichiometry, a controlled amount of TAA (150 mg), In $(NO_3)_3{\cdot}5H_2O$ (300 mg) and Zn $(acac)_2$ (130 mg) were dissolved in a mixture of 10 mL benzyl ether, 1,2 hexadecane diol (365 mg), oleic acid (1200 μL), oleyl amine (1225 μL). The result was mixed in and magnetically stirred under a flow of N_2 atmosphere for 20 min at room temperature. Then, the synthesized FePt core nanoparticles dissolved in 10 mL hexane were added to the reaction vessel to be mixed with other ingredients and magnetically stirred under a flow of N_2 atmosphere for 20 min at room temperature. For hexane evaporation, the reaction vessel was heated from room temperature to 100 °C for 20 min. Then, the mixture was heated from 100 °C to boiling point of benzyl ether (300 °C) at a rate of approximately 5 °C/min. After the reaction, the heat source was removed from the mixture allowing it to cool at room temperature. The core-shell nanostructures were filtrated and separated by adding 40 mL of ethanol and centrifugation in 8000 rpm for 10 min. At final, the obtained nanostructures dissolved in a mixture of oleic acid and oleyl amine in the presence of Hexane (10 mL) were centrifuged to separate impurities from synthesized nanoparticles.

2.5. Fabrication of FePt-$ZnIn_2S_4$@PGE

Firstly, the pencil graphite electrode (PGE) was polished on fine emery paper and then polished by slurry of alumina powder containing 0.05 μm grains of Al_2O_3. After this, the surface of electrode was rinsed with distilled water and dried at 25 °C. Then, 5 μL of the fine dispersed solution of the FePt-$ZnIn_2S_4$ nanoparticles in dimethylformamide (DMF) was dropped onto the surface of cleaned PGE and was dried in a hot air flow at 50 °C. After modification, the FePt-$ZnIn_2S_4$@PGE was washed with double distilled water, dried at room temperature and applied to electrochemical experiments. Scheme 1 shows summary of synthesis process and modifying the electrode using core shell nanostructures.

3. Results and discussions

3.1. Characterization of FePt, $ZnIn_2S_4$ and FePt-$ZnIn_2S_4$ nanostructures

Fig. 1a shows a TEM image of as-synthesized FePt nanoparticles. According to Fig. 1b, average diameter of FePt core particles ($\langle d \rangle$), based on log-normal fitting, is about 4.1 nm and standard deviation (σ) of about 0.36 nm, indicate narrow size distribution ($\sigma/\langle d \rangle$) of 0.09. Inset photography in Fig. 1b, shows HRTEM an image of a FePt particle which is highly spherical and mono dispersed.

Fig. 2(a–d) shows TEM and HRTEM images with different magnification of as-synthesized FePt/$ZnIn_2S_4$ core/shell nanoparticles which have also spherical shapes and are well isolated. HRTEM image of FePt/$ZnIn_2S_4$ (Fig. 2c and d) indicates that FePt cores are individually surrounded by $ZnIn_2S_4$ crystals.

Energy Dispersive Spectroscopy (EDS) analysis were employed to investigate the chemical composition of as-synthesized FePt and $ZnIn_2S_4$ nanostructures. The EDS profile of Fig. 2(e), reveals that equal atomic composition of FePt nanostructures, which is clear from the elemental peaks. The Peaks of element In, Zn and S are detected in the EDS profile (Fig. 2f). Atomic ratio of elements Zn:In:S is very close to 1:2:4, which is confirming the purity of the nanostructures.

Fig. 3A (a–c) shows the XRD patterns of FePt, $ZnIn_2S_4$ and FePt/$ZnIn_2S_4$ nanoparticles, respectively. As clearly can be seen, the pattern of FePt/$ZnIn_2S_4$ structure shows existence of two set peaks: one set is a chemically disordered fcc FePt phase and the other is hexagonal structured $ZnIn_2S_4$. The XRD peak intensities of Fig. 3A.c have been considerably decreased compared to Fig. 3A.a and A.b. Also the diffraction peaks of Fig. 3A.c are broader than the peaks of Fig. 3A.a and A.b. The reduction in peak intensities and peak broadness of the core/shell nanoparticles may be ascribed to the decrease of inter planer separation of crystal lattice. These results

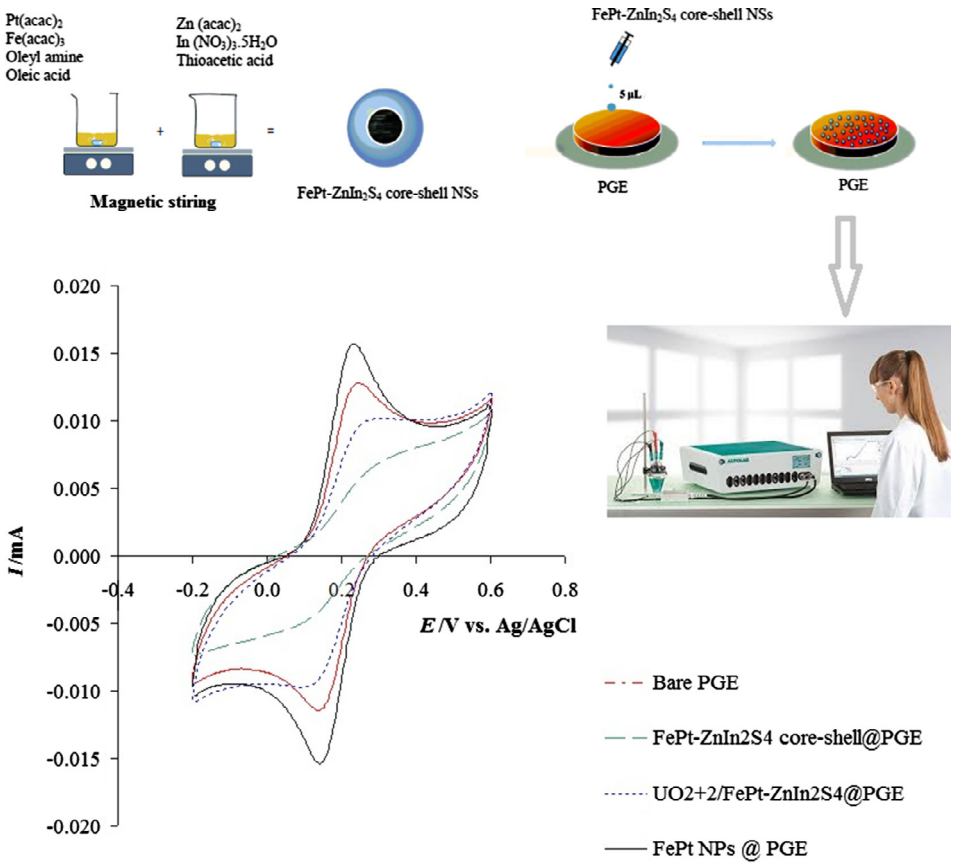

Scheme 1 Synthesis process and modifying the electrode using $FePt/ZnIn_2S_4$ core shell nanostructures.

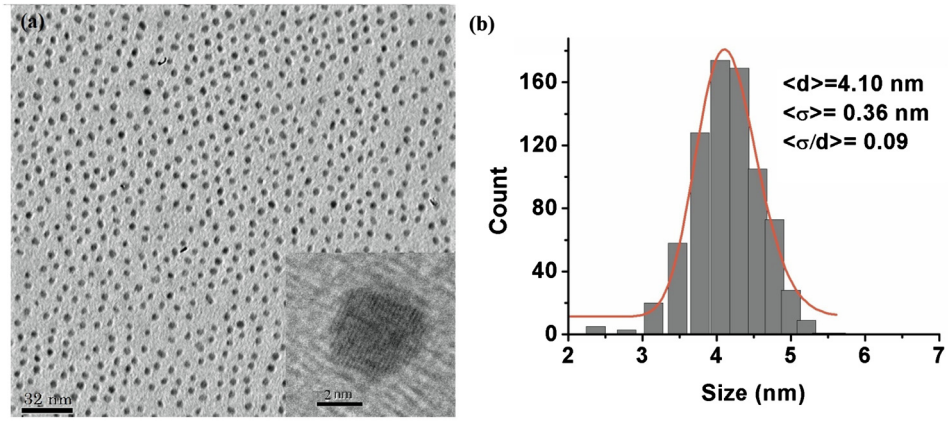

Fig. 1 (a) TEM image and (b) histogram of as-synthesized FePt nanoparticles with average size of 4.1 nm.

definitively showed that well defined $FePt/ZnIn_2S_4$ core/shell nanoparticles were successfully synthesized.

Fig. 3B.a-b shows the UV–Vis absorption spectra of the as-synthesized $ZnIn_2S_4$ and $FePt/ZnIn_2S_4$ core/shell nanoparticles. Both samples present strong similar absorption profiles with absorption edge at about 490 nm. From the absorption edge values, the corresponding band gap energy (E_g) for the $ZnIn_2S_4$ and $FePt/ZnIn_2S_4$ samples is 2.53 eV. The very slight shift of absorption edge for the $FePt/ZnIn_2S_4$ sample may be due to the large crystallite size and different particle morphology.

Temperature dependent hysteresis behavior of as-synthesized FePt and $FePt/ZnIn_2S_4$ showed super paramagnetic response at 300 K and ferromagnetic properties with a coercive field (H_c) of 2830 Oe and 970 Oe at 2 K, respectively. The coercivity values of FePt NPs drops sharply as temperature raised from 2 K to 4 K, 15 K and 20 K corresponding to 2830 Oe, 2130 Oe, 400 Oe and 160 Oe respectively, indicating that the size of the nanoparticles are thermally unstable. This is consistent with the low magneto crystalline anisotropy of fcc structure of the nanoparticles (Fig. 4A and C). The saturation magnetization of FePt is 1.65 emu/g at 300 K, which is

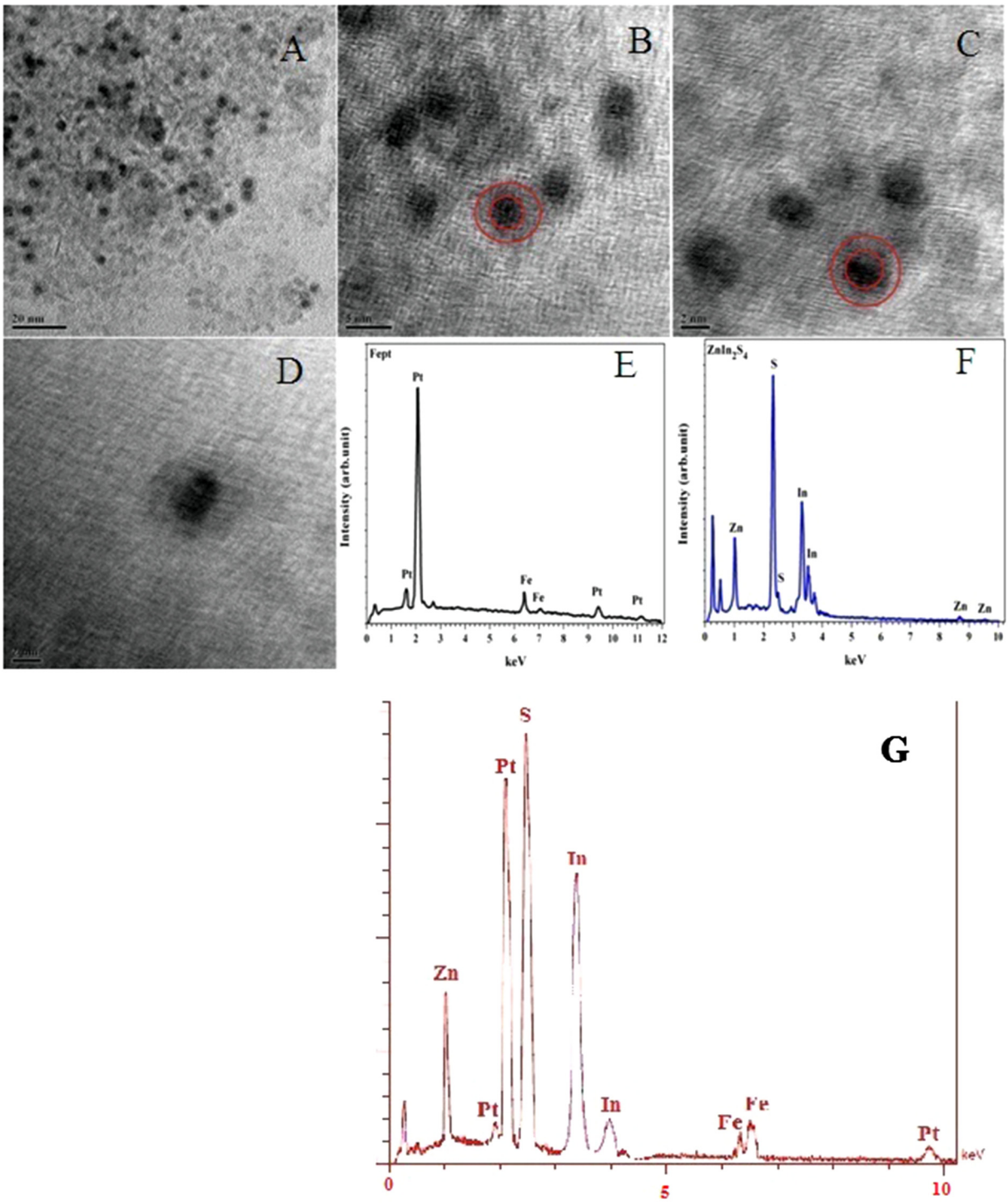

Fig. 2 (a)–(d) TEM and HRTEM images with different magnification of as-synthesized FePt/$ZnIn_2S_4$ core/shell nanoparticles. (e) and (f) EDXS profile of FePt and FePt/$ZnIn_2S_4$ core/shell, respectively.

much lower than the value of 7.73 emu/g at 2 K, being this is typical behavior of fcc FePt nanoparticles.

Temperature dependent magnetization in zero field cooled (ZFC) and field cooled (FC) of FePt and FePt/$ZnIn_2S_4$ NPs is shown in Fig. 4B and D. The blocking temperature (T_B) estimated by the peak in ZFC curve is about 26 K for FePt and about 46 K for FePt/$ZnIn_2S_4$ NPs. It indicates that $ZnIn_2S_4$ thin layer covers individual FePt NPs, which is consistent with the TEM and XRD results. Therefore inter particle separation increase in $ZnIn_2S_4$ coated FePt NPs, the reducing magnetic dipole-dipole interacting, this leads to a significant shift in T_B to higher temperature. Furthermore both ZFC-FC overlap a wide temperature range above T_B, meaning that the particles are non-interacting. The saturation magnetization of FePt/$ZnIn_2S_4$ NPs at 2 K decreased to 2.248 emu/g compared to FePt (7.73 emu/g), could be attributed to the presence of non

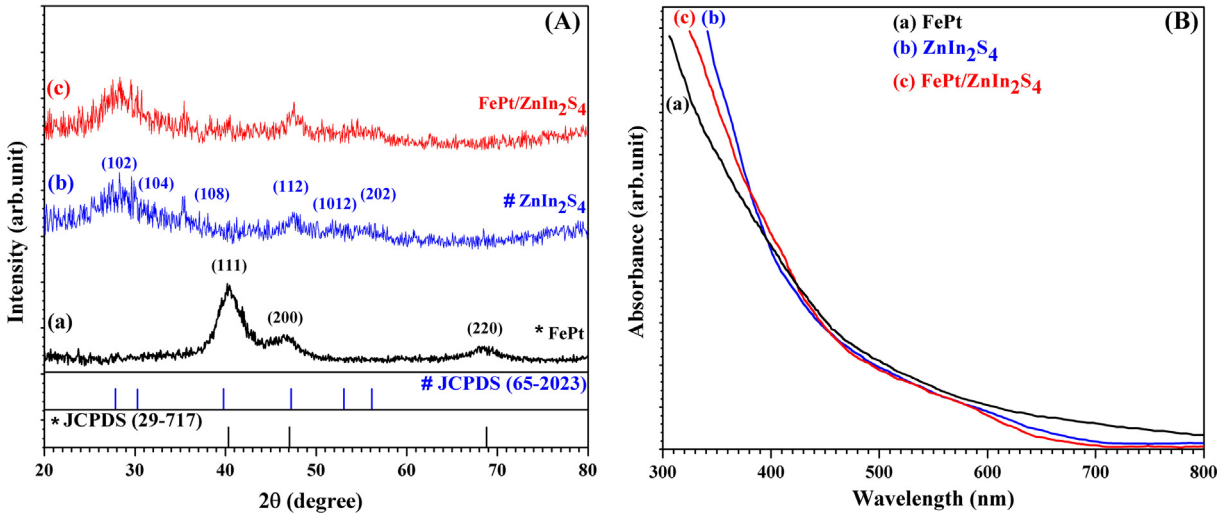

Fig. 3 (A) XRD patterns of as-synthesized nanoparticles (a) FePt, (b) $ZnIn_2S_4$, (c) $FePt/ZnIn_2S_4$. (B) UV–Vis absorption spectra of as-synthesized nanoparticles (a) $ZnIn_2S_4$, (b) $FePt/ZnIn_2S_4$.

magnetic $ZnIn_2S_4$ compound in the core/shell structure. The magnetic properties of as-synthesized FePt and $FePt/ZnIn_2S_4$ are summarized in Table 1 as extracted from Fig. 4(A–D).

3.2. Electrochemical application of FePt-$ZnIn_2S_4$ core-shell NSs

Cyclic voltammetry (CV) method was used to evaluate electrochemical behavior of different electrodes. So, CVs for 5.0 mM $Fe(CN)_6^{3-/4-}$ in 0.1 M phosphat buffer solution (PBS) on the bare PGE, FePt nanoparticles@PGE, FePt-$ZnIn_2S_4$ core-shell@PGE and UO_2^{2+}@FePt-$ZnIn_2S_4$ core-shell@PGE were drawn (Fig. 5). The quasi reversible one-electron redox behavior of ferricyanide ions was observed on the bare PGE with a peak separation (ΔE_p) of 0.086 V at the scan rate of 50 mV s^{-1}. After the modification of the electrode using FePt nanoparticles, the peak currents for $Fe(CN)_6^{3-/4-}$ increased about 1.37 times than for bare PGE, while the ΔE_p decreased (0.078 V). By immobilization of FePt-$ZnIn_2S_4$ core-shell nanostructures onto PGE, the peak current and peak potential unexpectedly changed for redox activity of $Fe(CN)_6^{3-/4-}$ at the surface of core-shell electrode. In this case, ΔE_p was found to be 0.177 V with reduced peak current about 4.2 times than bare PGE. The sharp decreasing in current can be due to the inhibitory effects of core-shell coating at the surface of electrode against diffusion of the probe ions to the surface of electrode. After the accumulation of uranyl ions on the surface of electrode, (UO_2^{2+}@FePt-$ZnIn_2S_4$ core-shell@PGE), the redox responses of $Fe(CN)_6^{3-/4-}$ was changed. The reason for small increase in faradic current observed for UO_2^{2+}@FePt-$ZnIn_2S_4$ core-shell@PGE in the presence of $[Fe(CN)_6]^{3-/4-}$ is a resultant of electrostatic attraction which exists between positively charged surface and negatively charged probe, and blocking effect of UO_2^{2+}@FePt-$ZnIn_2S_4$ core-shell with dominant effect of electrostatic attraction. These results are summarized in Table 2.

In an attempt to clarify the differences among the electrochemical performance of the bare PGE, FePt nanoparticles@PGE, FePt-$ZnIn_2S_4$ core-shell@PGE and UO_2^{2+}@FePt-$ZnIn_2S_4$ core-shell@PGE, electrochemical impedance spectroscopy (EIS) was used as a procedure to study electrodes surface. EIS is a suitable technique for investigation of the electrode surface dependent charge transfer process (interfacial properties, i.e., resistance and capacitance) (Bonanni et al., 2012; Bagheri et al., 2013). The experiments are done in $Fe(CN)_6^{3-/4-}$ redox probe by focus on the variations of the charge transfer resistance (R_{ct}) between solution and electrode surface. By immobilization of nanostructures in each step, the value of R_{ct} for modified electrode was changed. To construe data obtained from Nyquist plots, an equivalent circuit model was used to fit the results. In this circuit, R_s, Q and R_{ct} represent solution resistance, a constant phase element model parameter which is sometimes shown as Y_0 or T and named as double layer parameter and electron transfer resistance, respectively. W is a finite-length Warburg short-circuit term coupled to R_{ct}, which accounts for the Nernstian diffusion. In our work, the analysis of Nyquist plot showed a large decrease in R_{ct} at FePt nanoparticle@PGE compared to bare PGE in 0.1 M PBS solution (Fig. 6), indicating a significant increase in the rate of charge transfer. However, after fabrication of PGE with FePt-$ZnIn_2S_4$ core-shell, the semicircle increased distinctively, indicating that FePt-$ZnIn_2S_4$ core-shell could inhibited the electron transfer between the electrochemical probe $[Fe(CN)_6]^{3-/4-}$ and bare PGE (Fig. 6). With the accumulation of uranyl ions on the surface of the FePt-$ZnIn_2S_4$ core-shell@PGE, these ions act as an intermediary exchange of electrons between the $[Fe(CN)_6]^{3-/4-}$ and the surface of electrode. Therefore, by increasing the concentration of UO_2^{2+} onto core-shell nanostructures, gradually reduced charge transfers resistance. The results are summarized in Table 3.

3.3. pH optimization for accumulation of UO_2^{2+}

According to sensitivity of uranyl ions to the presence of phosphate ions in solution, the sodium acetate/acetic acid buffer solution was selected and optimized at pH = 4.0 for continue measurements which 0.025 M of sodium perchlorate ($NaClO_4$) was added to this solution to create the perfect environment

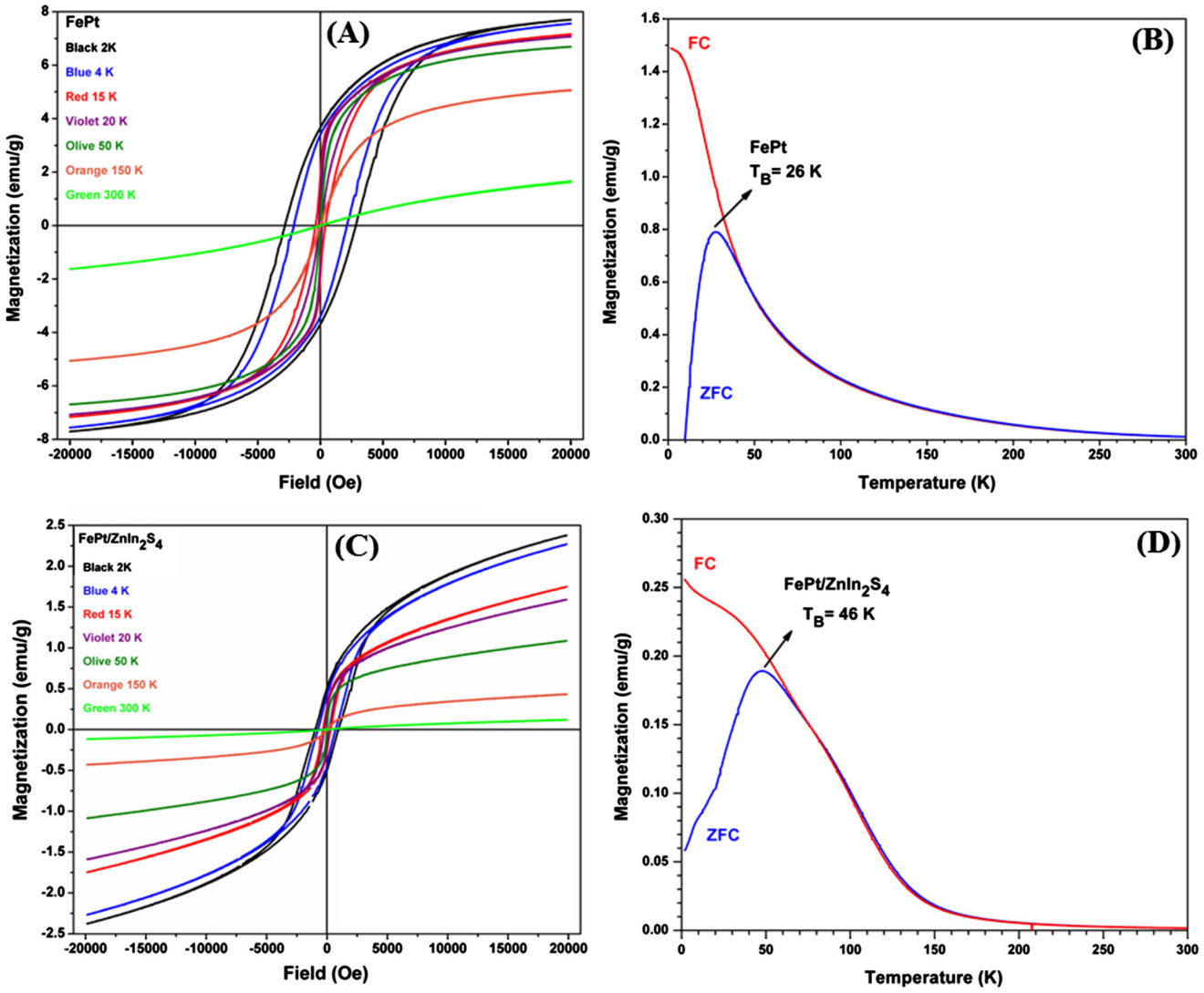

Fig. 4 (A) and (C) Temperature dependent hysteresis of as-synthesized FePt and FePt/$ZnIn_2S_4$. (B) and (D) Temperature dependent magnetization of as-synthesized FePt and FePt/$ZnIn_2S_4$.

Table 1 Magnetometry data obtained for the FePt and FePt/$ZnIn_2S_4$ nanoparticles: blocking temperature (T_B), magnetic coercivity (H_c), and saturation magnetization (M_s).

Sample	fcc-FePt	fcc Fet/$ZnIn_2S_4$
T_b	26 K	46 K
Hc @ 2 K (Oe)	2830	970
Hc @ 300 K (Oe)	0	0
M_S @ 2 K (emu/g)	7.73	2.24
M_S @ 300 K (emu/g)	1.65	0.11

for transferring and accumulation of uranyl ions from the bulk solution to the surface of modified electrode. Then, Nyquist plots were obtained in 0.1 M PBS in presence 5.0 mM $[Fe(CN)_6]^{3-/4-}$ probe from accumulation of 1.0 µM of UO_2^{2+} onto FePt-$ZnIn_2S_4$ core-shell@PGE at different pH values of 0.1 M sodium acetate/acetic acid buffer solution containing 0.025 M of sodium perchlorate. The R_{ct} of UO_2^{2+} @FePt-$ZnIn_2S_4$ core-shell@PGE was strongly depended upon pH of the pre-concentration solution and the best conditions was achieved around pH = 4.0.

3.4. Optimization of accumulation time

To optimize the accumulation time of UO_2^{2+} ions, the Nyquist plots of FePt-$ZnIn_2S_4$ core-shell@PGE against immersion time in UO_2^{2+} solution were draw in $[Fe(CN)_6]^{3-/4-}$ probe solution at the formal potential (*DC*, 0.25 V) and a frequency range of 0.1 Hz–100 kHz with an ac amplitude of 5.0 mV. Then, the changing procedure for charge transfer resistance (R_{ct}) of 5.0 mM $[Fe(CN)_6]^{3-/4-}$ at the UO_2^{2+} @FePt-$ZnIn_2S_4$ core-shell@PGE as a function of immersion time of the FePt-$ZnIn_2S_4$ core-shell@PGE electrode in UO_2^{2+} solution was investigated. According to results, a decreasing in R_{ct} was observed when the immersion time increases from 0 to 25 min, which in times longer, the charge transfer resistance did not change. Therefore, 25 min was chosen as the optimum

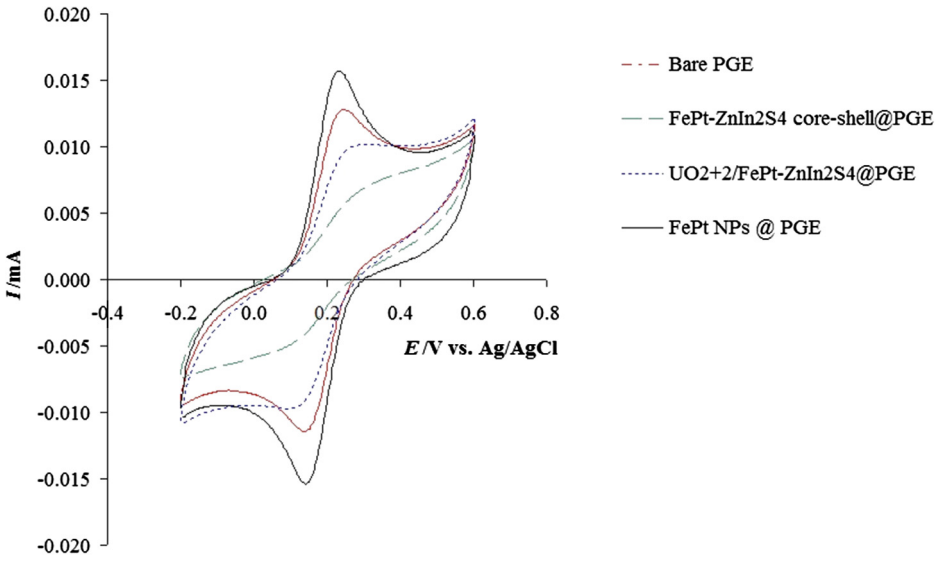

Fig. 5 CV curves of bare PGE, FePt NPs@PGE, FePt-$ZnIn_2S_4$ core-shell@PGE and UO_2^{2+}@FePt-$ZnIn_2S_4$ core-shell@PGE in the presence of 5.0 mM $Fe(CN)_6^{-3/-4}$ in 0.1 M PBS (pH = 6.0). Scan rate: 50 mV/s.

Table 2 Electrochemical parameters extracted from CV curves obtained on Bare-PGE and modified electrodes in the presence of 5.0 mM $Fe(CN)_6^{3-/4-}$ at pH 6.0 of 0.1 M PBS.

Electrode	E_a (V)	I_a (μA)	E_c (V)	I_c (μA)
Bare-PGE	0.237	8.85	0.150	−9.13
FePt NPs/PGE	0.228	12.11	0.150	−12.03
FePt-$ZnIn_2S_4$ @ PGE	0.282	2.11	0.105	−2.21
UO_2^{2+}@FePt-$ZnIn_2S_4$ @ PGE	0.253	5.424	0.134	−5.60

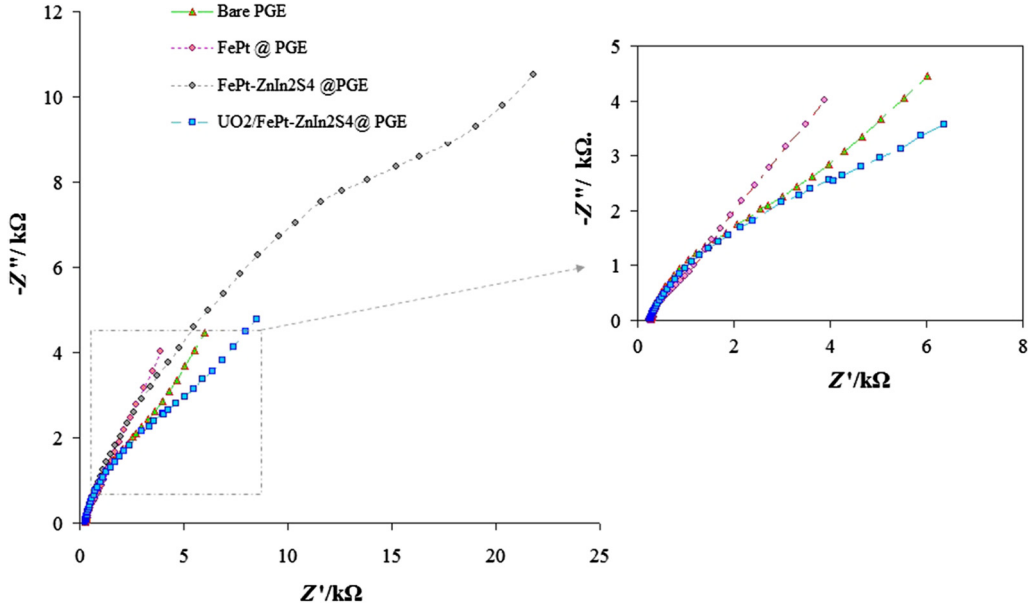

Fig. 6 Nyquist plots for bare PGE, FePt NPs@PGE, FePt-$ZnIn_2S_4$ core-shell@PGE and UO_2^{2+}@FePt-$ZnIn_2S_4$ core-shell@PGE in the presence of 5.0 mM $Fe(CN)_6^{3-/4-}$ in 0.1 M PBS (pH = 6.0). Conditions: *DC* potential, +250 mV; ac amplitude, 5.0 mV; frequency range: 10 kHz-100 mHz.

Table 3 Electrochemical parameters extracted from Nyquist plots obtained on different PGEs in the presence of 5.0 mM $Fe(CN)_6^{3-/4-}$ at pH 6.0 of 0.1 M PBS.

Electrode	R_s (Ω)	R_{ct} (Ω)	Q (s^n Ω^{-1})		W
			Y_0	n	
Bare-PGE	267.76	2908.9	3.26×10^{-5}	0.824	2.03×10^{-4}
FePt NPs @ PGE	244.89	564.2	9.39×10^{-6}	0.904	2.26×10^{-4}
FePt-$ZnIn_2S_4$ @ PGE	265.21	18723	6.47×10^{-6}	0.733	3.06×10^{-4}
UO_2^{2+}@FePt-$ZnIn_2S_4$ @ PGE	253.46	5303.6	2.55×10^{-5}	0.710	1.85×10^{-4}

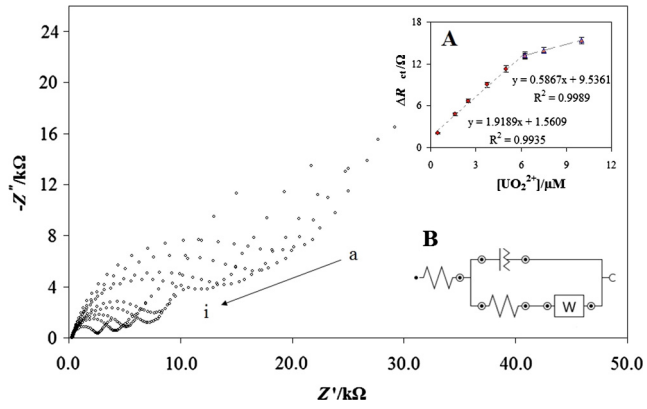

Fig. 7 Nyquist plots obtained for the faradaic impedance measurements on FePt-$ZnIn_2S_4$ core-shell@PGE after incubation of the electrode for 25 min in various concentrations of UO_2^{2+}; a-i corresponds to: 0.0, 0.5, 1.62, 2.5, 3.75, 5.0, 6.25, 7.5 and 10.0 μM of UO_2^{2+}. (A) Variation of charge transfer resistance (ΔR_{ct}) versus various concentrations of UO_2^{2+} and (B) the equivalent circuit used in the fit procedure of the impedance spectra.

immersion/accumulation time for adsorption of UO_2^{2+} in this work.

3.5. Calibration curve and limit of detection for UO_2^{2+}

The EIS measurements obtained under the optimized conditions at a constant DC potential of +0.25 V vs. Ag/AgCl reference electrode on FePt-$ZnIn_2S_4$ core-shell@PGE, after accumulation of UO_2^{2+} from solutions containing different concentrations of UO_2^{2+} are presented in Fig. 7. The charge transfer resistance of modified electrode was decreased by increasing the UO_2^{2+} concentrations in accumulation solution (Fig. 7A). With approximating experimental data using [R(Q[RW])] as CPE model (Fig. 7B), the values of R_{ct} and other parameters were extracted. These behaviors allowed constructing of the calibration curve for determination of UO_2^{2+}. Two linear calibration curve $\Delta R_{ct}/\Omega = 1918.9\ [UO_2^{2+}] + 1560.9$, $R^2 = 0.9935$ from 0.5 to 6.25 μM UO_2^{2+} and $\Delta R_{ct}/\Omega = 586.6\ 9\ [UO_2^{2+}] + 9536.1$, $R^2 = 0.9989$ from 6.25 to 10.0 μM UO_2^{2+} and a detection limit of 71.7 nM was found by using ΔR_{ct} as a function of UO_2^{2+}, where $\Delta R_{ct} = R_{ct\ in\ UO2=0} - R_{ct\ in\ UO2=x}$. To compare among our paper and other papers, it is important that investigated several parameters simultaneously; novelty of sensor (No papers have yet been reported for application of core shell nanostructures in dedection of uranyl ions.), detection limit, linear rang of calibration curve, simplicity for preparation, selectivity and sensitivity of electrode. With comparison between these factors, it seems that this modified electrode has novelty with agreeable detection limit, selectivity than to other cations as interferences and agreeable dynamic range for uranyl against other reported papers. Table 4 shows summary of this comparison. Also, The relative standard deviations of ΔR_{ct} as 1.32% (n = 4) were found for 1.5 μM UO_2^{2+}, respectively, which is very small implying the repeatability of the electrode response obtained by using EIS method.

3.6. Interference study and real sample analysis

To evaluate the ability of FePt-$ZnIn_2S_4$ core-shell@PGE in sensing of UO_2^{2+} ions, the effect of some cations and anions, such as Pb^{2+}, K^+, NH_4^+, Ni^{2+}, Zn^{2+}, Mn^{2+}, Cu^{2+}, $Cr_2O_7^{2-}$, CO_3^{2-}, Cl^- and SO_4^{2-} was investigated.

Table 4 Comparison of present work with some reported methods used in the determination of UO_2^{2+} based on efficiency.

Sensor	Detection method	Limit of detection	Linear dynamic range	Ref
Uranyl ionic imprinted polymer	Potentiometric	1.0 μM	3.0–6000 1 μM	Abu-Dalo et al. (2016)
6-O-palmitoyl-l-ascorbic acid (PAA)-modified graphite (GRA) electrode	Differential pulse voltammetry (DPV)	1.8 μg L^{-1}	2.7–67.5 μg L^{-1}	Dimovasilis and Prodromidis (2011)
Carboxylated graphene modified Glassy carbon electrode	DPV	130 nM	0.05–5. 0 μM	Ziółkowski et al. (2017)
Tetraphenylethene-based fluorescent sensor	Colorimetric	–	1.0–20.0 μM	Wena et al. (2016)
$POCl_3$/mercapto ethanol/Au	Square wave voltammetry	< 1 μM	1.0–10.0 μM	Becker et al. (2009)
PBED optical sensor	Spectrophotometery	0.999 μM	3.99–80.6 μM	Ghaedi et al. (2012)
FePt-$ZnIn_2S_4$ core-shell@PGE	EIS	71.7 nM	0.5–10.0 μM	This work

Table 5 Determination of UO_2^{2+} ions in watery samples based on standard addition method.

Sample	Added (μM)	Found (μM)	Recovery (%)	Recovery standard deviation	Content of sample (μM)
Synthetic sample					
(I)	1.00	2.96	98.0	0.03	2.0
(II)	4.50	9.70	96.3	0.14	5.4
Mineral water	2.00	1.95	97.0	0.07	No or < LOD

In accordance to the ±5.0% relative error (Honarmand et al., 2016), the interferences ions did not show any negative impact on the measurement of ions uranyl. These results indicated that under optimized conditions, the selective and sensitive determination of UO_2^{2+} ions could be possible in spiked samples at the FePt-$ZnIn_2S_4$ core-shell@PGE. Therefore, the recovery tests were measured based on standard addition method by spiking different concentrations of UO_2^{2+} solution into watery samples. Recoveries were found to be 96.3 and 98.0% for 2.0 μM UO_2^{2+}, respectively. The obtained results were summarized in Table. 5.

4. Conclusions

Solvothermal method was used for the synthesis of FePt core, $ZnIn_2S_4$ shell and FePt $ZnIn_2S_4$ core-shell nanostructures in the presence of 1,2-hexadecanediol, oleyl amine and amyl alchol as a reducing agents. According to chemical affinity of modified electrode to uranyl ion adsorption, the FePt $ZnIn_2S_4$ core-shell@PGE was fabricated and applied for measuring of uranyl cations. So, by accumulation of UO_2^{2+} from solutions containing different concentrations of UO_2^{2+}, a detection limit of 71.7 nM of UO_2^{2+} was found by EIS method. The RSD in peak current (1.32%, n = 4) for modified electrode shown good repeatability of modified electrode in absorbance of UO_2^{2+}.

Acknowledgment

This work was supported by the Islamic Azad University Kashan Branch. Access to TAIL-UC facility funded under QREN-Mais Centro Project ICT-2009-02-012-1890 is gratefully acknowledged.

References

Abu-Dalo, M.A., Al-Rawashdeh, N.A.F., Al-Mheidat, I.R., Nassory, N.S., 2016. Preparation and evaluation of new uranyl imprinted polymerelectrode sensor for uranyl ion based on uranyl–carboxybezotriazolecomplex in pvc matrix membrane. Sens. Actuat. B 227, 336–345.

Bagheri, H., Afkhami, A., Khoshsafar, H., Rezaei, M., Shirzadmehr, A., 2013. Simultaneous electrochemical determination of heavy metals using a triphenylphosphine/MWCNTs composite carbon ionic liquid electrode. Sens. Actuat. B 186, 451–456.

Balamurugan, A., Ho, K.C., Chen, S.M., Huang, T.Y., 2011. Electrochemical sensing of NADH based on Meldola Blue immobilized silver nanoparticle-conducting polymer electrode. Colloids Surf. A 362, 1–7.

Becker, A., Tobias, H., Mandler, D., 2009. Electrochemical determination of uranyl ions using a self-assembled monolayer. Anal. Chem. 81, 8627–8631.

Bonanni, A., Loo, A.H., Pumera, M., 2012. The application of graphene for *in vitro* and *in vivo* electrochemical biosensing. Trends Anal. Chem. 37, 12–19.

Bozhko, V.V., Novosad, A.V., Davidyuk, G.E., Kozer, V.R., Parasyuk, O.V., Vainorius, N., Janonis, V., Sakavicius, A., Kazukauskas, V., 2013. Electrical and photoelectrical properties of $CuInS_2$-$ZnIn_2S_4$ solid solutions. J. Alloys Comp. 553, 48–52.

Byrne, A.R., Benedik, L., 1988. Determination of uranium at trace levels by radiochemical neutron-activation analysis employing radioisotopic yield evaluation. Talanta 35, 161–166.

Carvajal, C.G., Snow Davis, C., Mundle, R., Pradhan, A.K.V.L.S., 2014. Growth of highly oriented SnO_2 nanorods and ZnO hybrid films for gas sensing measurements. J. Electrochem. Soc. 161, B3151–B3154.

Chai, B., Peng, T.Y., Zeng, P., Zhang, X.H., 2012. Preparation of a MWCNTs/$ZnIn_2S_4$ composite and its enhanced photocatalytic hydrogen production under visible-light irradiation. Dalton Trans. 41, 1179–1186.

Chen, J., Zhang, H., Liu, P., Li, Y., Liu, X., Li, G., Wong, P.K., An, T., Zhao, H., 2015. Cross-linked $ZnIn_2S_4$/rGO composite photocatalyst for sunlight-driven photocatalytic degradation of 4-nitrophenol. Appl. Catal. B 168, 266–273.

Cheng, J.P., Wang, B.B., Zhao, M.G., Liu, F., Zhang, X.B., 2014. Nickel-doped tin oxide hollow nanofibers prepared by electrospinning for acetone sensing. Sens. Actuat. B 190, 78–85.

Chi, X., Liu, C., Liu, L., Li, Y., Wang, Z., Bo, X., 2014. Tungsten trioxide nanotubes with high sensitive and selective properties to acetone. Sens. Actuat. B 194, 33–37.

Davis, W., Gray, W., 1964. A rapid and specific titrimetric method for the precise determination of uranium using iron (II) sulphate as reductant. Talanta 11, 1203–1211.

Dimovasilis, P.A., Prodromidis, M.I., 2011. An electrochemical sensor for trace uranium determination based on 6-O-palmitoyl-l-ascorbic acid-modified graphite electrodes. Sens. Actuat. B 156, 689–694.

Dotzauer, D.M., Dai, J.H., Sun, L., Bruening, M.L., 2006. Catalytic membranes prepared using layer-by-layer adsorption of polyelectrolyte/metal nanoparticle films in porous supports. Nano Lett. 6, 2268–2272.

Ejnik, J.W., Carmichael, A.J., Hamilton, M.M., McDiarmid, M., Squibb, K., Boyd, P., Tardiffs, W., 2000. Determination of the isotopic composition of uranium in urine by inductively coupled plasma mass spectrometry. Health Phys. 78, 143–148.

Fang, Y.L., Zhang, A., Wang, H., Li, H., Zhang, Z.W., Chen, S.X., Luan, L.Y., 2010. Health risk assessment of trace elements in Chinese raisins produced in Xinjiang province. Food Control 21, 732–739.

Fujino, O., Umetani, S., Ueno, E., Shigeta, K., Matsuda, T., 2000. Determination of uranium and thorium in apatite minerals by inductively coupled plasma atomic emission spectrometry with solvent extraction separation into diisobutyl ketone. Anal. Chim. Acta 420, 65–71.

Ghaedi, M., Tashkhourian, J., Montazerozohori, M., Amiri Pebdani, A., Khodadoust, S., 2012. Design of an efficient uranyl ion optical sensor based on 1′-2,2′-(1,2-phenylene)bis(ethene-2,1-diyl)dinaphthalen-2-ol. Mater. Sci. Eng. C 32, 1888–1893.

Grudpan, K., Laivoraungrath, S., Sooksamifi, P., 1995. Flow injection spectrophotometric determination of uranium with in-valve ion-

exchange column preconcentration and separation. Analyst 120, 2107–2110.
Hieu, N.T., Baik, S.J., Chung, O.H., Park, J.S., 2014. Fabrication and characterization of electrospun carbon nanotubes/titanium dioxide nanofibers used in anodes of dye-sensitized solar cells. Synth. Met. 193, 125–131.
Honarmand, E., Motaghedifard, M.H., Hadi, M., Mostaanzadeh, H., 2016. Electro-oxidation study of promethazine hydrochloride at the surface of modified gold electrode using molecular self assembly of a novel bis-thio Schiff base from ethanol media. J. Mol. Liquid 216, 429–439.
Hong, K.B., Jung, K.W., Jung, K.H., 1989. Application of laser-induced fluorescence for determination of trace uranium, europium and samarium. Talanta 36, 1095–1099.
Khan, M.H., Ali, A., Khan, N.N., 2001. Spectrophotometric determination of thorium with disodium salt of arsenazo-III in perchloric acid. J. Radioanal. Nucl. Chem. 353, 353–357.
Khan, M.H., Yasmin, N., 2003. Study of metallic pollutants in water and food items of an industrial city by atomic absorption spectrophotometry. Pakistan J. Biol. Sci. 6, 1276–1281.
Khayatian, A., Kashi, M.A., Azimirad, R., Safa, S., 2014. Enhanced gas-sensing properties of ZnO nanorods encapsulated in an Fe-doped ZnO shell. J. Phys. D Appl. Phys. 47, 075003–075009.
Lei, Z.B., You, W.S., Liu, M.Y., Zhou, G.H., Takata, T., Hara, M., Domen, K., Li, C., 2003. Photocatalytic water reduction under visible light on a novel $ZnIn_2S_4$ catalyst synthesized by hydrothermal method. Chem. Commun. 39, 2142–2143.
Li, P., Feng, X.B., Qiu, G.L., Shang, L.H., Li, Z.G., 2009. Mercury pollution in Asia: a review of the contaminated sites. J. Hazard. Mater. 168, 591–601.
Li, J., Zhang, Y., 2012. Remediation technology for the uranium contaminated environment: a review. Proc. Environ. Sci. 13, 1609–1615.
Lu, B.F., Liu, L.B., Cheng, J.K., 1998. Separation and determination of thorium, uranium and mixed rare-earth elements as their UV/Vis absorbing complexes by capillary zone electrophoresis. Talanta 47, 291–299.
Mei, Z.W., Ouyang, S.X., Tang, D.M., Kako, T., Golberg, D., Ye, J. H., 2013. An ion-exchange route for the synthesis of hierarchical $In_2S_3/ZnIn_2S_4$ bulk composite and its photocatalytic activity under visible-light irradiation. Dalton Trans. 42, 2687–2690.
Peng, S., Zhu, P., Thavasi, V., Mhaisalkar, S.G., Ramakrishna, S., 2011. Facile solution deposition of $ZnIn_2S_4$ nanosheet films on FTO substrates for photoelectric application. Nanoscale 3, 2602–2607.
Romeo, N., Dallaturca, A., Braglia, R., Sberveglieri, G., 1973. Charge storage in $ZnIn_2S_4$ single crystals. Appl. Phys. Lett. 22, 21–27.
Seo, W.S., Otsuka, R., Okuno, H., Ohta, M., Koumoto, K., 1999. Thermoelectric properties of sintered polycrystalline $ZnIn_2S_4$. J. Mater. Res. 14, 4176–4181.
Shen, S.H., Zhao, L., Zhou, Z., 2008. Enhanced photocatalytic hydrogen evolution over Cu-doped $ZnIn_2S_4$ under visible light irradiation. J. Phys. Chem. C 112, 16148–16155.
Shim, Y.S., Moon, H.G., Kim, D.H., Zhang, L., Yoon, S.J., Yoon, Y. S., 2013. Au-decorated WO_3 cross-linked nanodomes for ultrahigh sensitive and selective sensing of NO_2 and C_2H_5OH. RSC Adv. 3, 10452–10459.
Wang, X., Fan, H., Ren, P., 2013. Electrospinning derived hollow SnO_2 microtubes with highly photocatalytic property. Catal. Commun. 31, 37–41.
Wena, J., Huanga, Z., Hua, S., Lib, S., Lic, W., Wang, X., 2016. Aggregation-induced emission active tetraphenylethene-based sensor for uranyl ion detection. J. Hazard. Mater. 318, 363–370.
Xing, L.L., Yuan, S., Chen, Z.H., Chen, Y.J., Xue, X.Y., 2011. Enhanced gas sensing performance of SnO_2/α-MoO_3 heterostructure nanobelts. Nanotechnology 22, 225502–225508.
Yan, X., Liu, H., Liew, K.Y., 2001. Size control of polymer-stabilized ruthenium nanoparticles by polyol reduction. J. Mater. Chem. 11, 3387–3391.
Yu, Y.G., Chen, G., Wang, G., Lv, Z.S., 2012. Visible-light-driven $ZnIn_2S_4/CdIn_2S_4$ composite photocatalyst with enhanced performance for photocatalytic H_2 evolution. Int. J. Hydrogen Energy 38, 1278–1285.
Yuan, W.H., Liu, X.C., Li, L., 2013. Improving photocatalytic performance for hydrogen generation over Co-doped $ZnIn_2S_4$ under visible light. Acta Phys. Chim. Sin. 29, 151–156.
Zhou, J., Tian, G., Chen, Y., Meng, X., Shi, Y., Cao, X., Pan, K., Fu, H., 2013. In situ controlled growth of $ZnIn_2S_4$ nanosheets on reduced graphene oxide for enhanced photocatalytic hydrogen production performance. Chem. Commun. 49, 2237–2239.
Ziółkowski, R., Górski, Ł., Malinowska, E., 2017. Carboxylated graphene as a sensing material for electrochemicaluranyl ion detection. Sens. Actuat. B 238, 540–547.